Fabrication of flexible all-inorganic nanocrystal solar cells by room-temperature processing†‡

Anna Loiudice,[ab] Aurora Rizzo,[*bc] Giulia Grancini,[d] Mariano Biasiucci,[e] Maria R. Belviso,[c] Michela Corricelli,[fg] M. Lucia Curri,[f] Marinella Striccoli,[f] Angela Agostiano,[gf] P. Davide Cozzoli,[ac] Annamaria Petrozza,[d] Guglielmo Lanzani[dh] and Giuseppe Gigli[abc]

We demonstrate the fabrication of all-inorganic heterostructured n–p junction devices made of colloidal PbS quantum dots (QDs) and TiO_2 nanorods (NRs). The entire device fabrication procedure relies on room-temperature processing, which is compatible with flexible plastic substrates and low-cost production. Through Kelvin Probe Force Microscopy and femtosecond pump and probe spectroscopy we decipher the electron transfer process occurring at the interface between the colloidal PbS QDs and TiO_2 anatase NRs. Overall we demonstrate a high power conversion efficiency of ∼3.6% on glass and ∼1.8% on flexible substrates, which is among the highest reported for entirely inorganic-nanocrystal based solar cells on plastic supports.

Broader context

Solution processed-colloidal nanocrystals (NCs) offer the potential to fabricate solar cells on large areas at low cost and with improved efficiency. Their wide spectral tunability, originating from the quantum size effect, may enable efficient light harvesting of the entire solar energy spectrum spanning across the visible and infrared regions. In this paper, we report on the fabrication of high-efficiency all-inorganic solar cells by a novel approach that involves processing of colloidal PbS QDs and anisotropic TiO_2 NCs under room-temperature conditions. Our results fully meet one of the major pursued goals in the design and fabrication of NC-based solar cells, that is the development of a facile and mild-room temperature solution-based route for the assembly of solar cells *via* utilization of "inorganic inks" that combine the advantages of low-temperature solution-processable organic compounds and the chemical–physical properties of semiconductor NCs.

Introduction

In the quest for high efficiency energy sources, recent breakthroughs in the realization of solar cells that exploit

[a]Dipartimento di Matematica e Fisica ʹE. De Giorgiʹ, Università del Salento, via per Arnesano, 73100 Lecce, Italy

[b]CBN – Center for Biomolecular Nanotechnologies, Italian Institute of Technology, Energy Platform, Via Barsanti sn, 73010 Arnesano, Lecce, Italy. E-mail: aurora.rizzo@nano.cnr.it; Fax: +39-0832-298237; Tel: +39-0832-298211

[c]NNL CNR-Istituto Nanoscienze, c/o Distretto Tecnologico, via per Arnesano km. 5, 73100 Lecce, Italy

[d]Center for Nano Science and Technology @ PoliMi, Istituto Italiano di Tecnologia, Via Pascoli 70/3, 20133 Milano, Italy

[e]Center for Life Nano Science@Sapienza, Istituto Italiano di Tecnologia, Viale Regina Elena 291, 00161 Roma, Italy

[f]Istituto per i Processi Chimico Fisici (IPCF-CNR) Bari, c/o Department of Chemistry, Via Orabona 4, I-70126 Bari, Italy

[g]Department of Chemistry, University of Bari, Via Orabona 4, I-70126 Bari, Italy

[h]Dipartimento di Fisica, Politecnico di Milano, Piazza L. da Vinci, 32, 20133 Milano, Italy

† Dedicated to the memory of Dr. Gianluca Latini, who passed away in March 2012.

‡ Electronic supplementary information (ESI) available. See DOI: 10.1039/c3ee23928d

wet-chemically prepared nanocrystals (NCs) as active functional elements have drawn the attention of the scientific community to such nanomaterials.[1–6] Solution-grown semiconductor NCs stand out over traditional photovoltaic nanomaterials due to the flexibility with which they can be synthesized with controlled composition and the ease with which they can be processed for device-fabrication purposes, retaining their inherent size-tunable broadband absorption features and superior transport properties.[7,8] The most efficient NC-based system for photovoltaic application consists of low band gap PbS quantum dots (QDs) as the light harvester coupled with transition-metal oxide TiO_2 as the electron acceptor.[9] These devices have been developed into various configurations, spanning from bi-layer heterostructures[10] to depleted bulk heterojunctions,[11] which have allowed reaching a state of the art power conversion efficiency of 6–7%.[12–14] Despite the tremendous improvement in performance achieved over other donor/acceptor NC systems, PbS QDs/TiO_2 solar cells remain far less appealing for potential implementation in flexible plastic technology and large-scale industrial manufacturing because the preparation of the relevant TiO_2 acceptor film usually requires harsh high-temperature processing. Indeed the vast

This journal is © The Royal Society of Chemistry 2013

Energy Environ. Sci., 2013, **6**, 1565–1572 | **1565**

majority of studies on PbS QDs/TiO$_2$ photovoltaic devices exhibiting solar power conversion efficiencies greater than 3% have relied on annealing TiO$_2$ electrodes at temperatures of 500 °C or higher.[15] Such thermal treatments are essential to convert the non-stoichiometric amorphous TiO$_x$, derived from a sol–gel deposition reaction, into a crystalline anatase phase and to remove any associated organic components. Some examples of NC solar cells prepared at lower temperature (<300 °C) have been reported for other systems, such as ZnO/PbS, PbS/Bi$_2$S$_3$, and CdTe/CdSe.[16–18]

Herein, we report on the fabrication of high-efficiency all-inorganic solar cells by a novel approach that involves processing of colloidal PbS QDs and anisotropic TiO$_2$ NCs under room-temperature conditions. Our heterostructured device is made of a PbS QD layer, which absorbs light in the VIS–near IR region, interfaced to a film of crystalline nanorods (NRs) of anatase TiO$_2$. Charge separation occurs at the interface, allowing the as-separated electrons and holes to be transported through the metal oxide and the PbS layers, respectively. The use of preformed TiO$_2$ NRs avoids the application of a high-temperature annealing step to obtain the oxide in the required crystalline form. In addition, gentle post-deposition processing routes, which are based on mild acidic treatments of PbS QDs[9] and UV-light irradiation of TiO$_2$ NRs,[19] respectively, are exploited to remove the insulating capping surfactants from the NC surface at room-temperature. Through these procedures we have realized solar cell devices that achieve a power conversion efficiency of ~3.6% on glass and ~1.8% on polyethylene terephthalate (PET) substrates, which are among the highest reported for entirely inorganic-NC-based solar cells on a plastic support.[20] In addition, we support our achievements with fundamental studies performed by Kelvin Probe Force Microscopy (KPFM) measurements and femtosecond transient absorption to monitor the charge generation mechanism which governs the device performance. Overall, our results fully meet one of the major and intensively pursued goals in the design and fabrication of photovoltaic NC-based materials, that is the development of a facile and mild-room temperature solution-based route for the assembly of solar cells *via* utilization of "inorganic inks" that combine the advantages of low-temperature solution-processable organic compounds, on one side, and the chemical–physical properties of colloidal semiconductor NCs on the other side. Therefore, the applicability of our approach to the straightforward fabrication of photovoltaic devices on flexible plastic substrates represents a considerable step forward in the search for high-efficiency energy sources under low-cost processing conditions.

Result and discussion

TiO$_2$/PbS nanocrystal based devices

In Fig. 1a–c we show representative transmission electron microscopy (TEM) images and absorption spectra of the PbS QDs and TiO$_2$ NRs used to construct our devices, together with a sketch of the expected energy band diagram. The TiO$_2$ NRs were synthesized by means of an advanced surfactant-assisted sol–gel route starting from a titanium alkoxide precursor, which
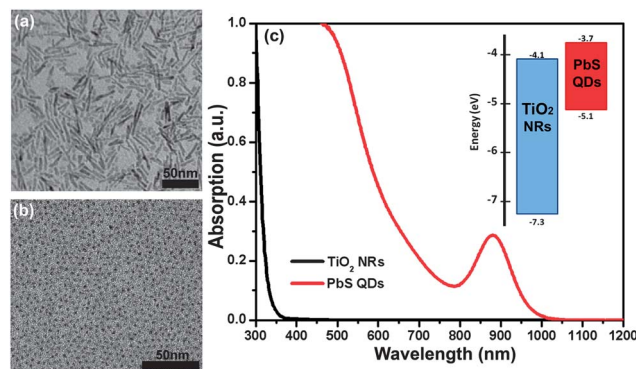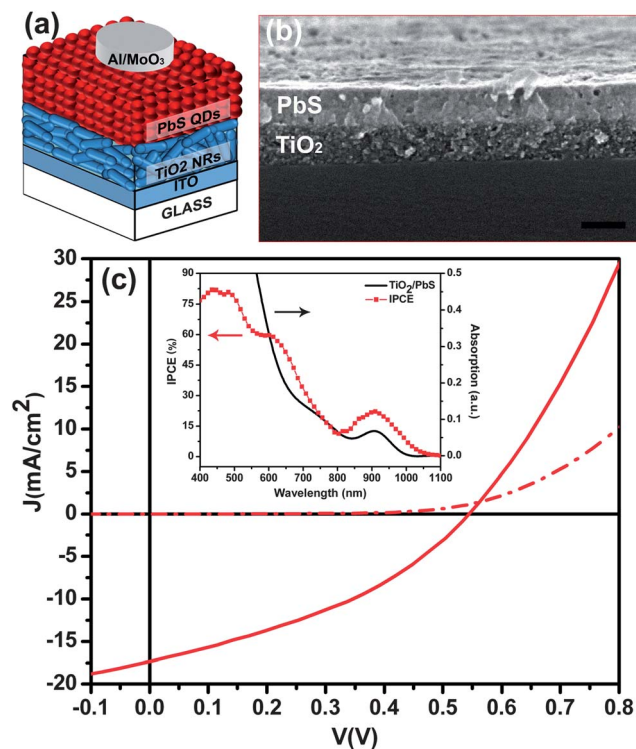

Fig. 1 TEM images of (a) TiO$_2$ NRs and (b) PbS QDs; (c) normalized absorption of TiO$_2$ and PbS NCs in solution. Inset: schematic sketch of the energy level diagram of the TiO$_2$-NR–PbS-QD bi-layer.[21]

allowed us to obtain anisotropic crystalline nanoparticles with mean short/long axis dimensions of 4–5 nm/20–40 nm, respectively, in the pure anatase phase.[21]

The organic capped PbS QDs are prepared following a modified literature procedure based on the surfactant-assisted pyrolysis of organometallic precursors,[22,23] which allowed facile tuning of the optical band gap *via* NC size control. As PbS QDs exhibit a broad absorption over the entire solar spectrum, they allow the solar cell sensitivity to be extended to the infrared radiation. For the purposes of the present work, we synthesized monodisperse, nearly spherical PbS QDs with a diameter of 2.8 ± 0.5 nm, as determined from the TEM micrographs. The estimated size value was in good agreement with the theoretical value,[24] which corresponds to an optical absorption spectrum in toluene solution with the first 1S exciton feature at 880 nm (see Fig. 1c). The as-synthesized NCs were capped with an insulating organic layer of surfactants (OLAC and OLAC/TOP in the case of TiO$_2$ and PbS, respectively), which exposed long alkyl chains outwards, thus ensuring full NC solubility in organic solvents.

The energy level alignment of PbS QDs and TiO$_2$ NRs sketched in Fig. 1c is taken from previously published reports.[25] Considering the values reported in the literature for the 1S electron level of PbS QDs with this diameter and the conduction band of nanocrystalline TiO$_2$, we expect photoinduced electron transfer from PbS to TiO$_2$ to be energetically allowed. Accordingly, we have fabricated devices with inverted geometry (Fig. 2a) consisting of ITO/TiO$_2$-NRs/PbS-QDs/MoO$_3$/Al, where electrons and holes are extracted through the TiO$_2$ at the ITO and through the MoO$_3$ at the Al contacts, respectively. The n–p junction is formed between p-type PbS QDs and n-type TiO$_2$ NR supports. The built-in field leads to separation of the electrons to the n-type TiO$_2$ and the holes to the p-type PbS QDs at the interface.

In more detail, the TiO$_2$ NRs can be easily processed into a thin film *via* spin-coating onto indium tin oxide (ITO) substrates, forming a smooth and homogeneous film.[19] The long alkyl chain oleate ligands are eliminated by exposing the film to a cw-UV lamp at room-temperature in air. In this way we obtain a twofold improvement. Firstly, we increase film conductivity by enhancing inter-nano crystal coupling, which

1566 | *Energy Environ. Sci.*, 2013, **6**, 1565–1572

This journal is © The Royal Society of Chemistry 2013

Fig. 2 (a) Sketch of the device and (b) cross-sectional SEM image of the TiO$_2$–PbS bi-layer on the Si/SiO$_2$ substrate. The scale bar is 100 nm. The TiO$_2$ layer is formed by disordered assemblies of NRs, as can be observed in Fig. S1 of the ESI‡ (c) Current density *vs.* applied bias (*J–V*) characteristics under AM1.5 G (100 mW cm^{-2}) simulated solar illumination (solid line) and in the dark (dash-dotted line) for the TiO$_2$-NR/PbS-QD based solar cells. Inset: IPCE spectrum for the same device and normalized absorption spectrum of the TiO$_2$-NR–PbS-QD bi-layer.

would otherwise be reduced by the potential barriers caused by the original surface ligands. Secondly, we prevent possible solubilization of the NRs into the nonpolar solvents used for the subsequent layer depositions. This allows employment of a sequential spin-coating and UV-irradiation method to obtain thick, crack-free, and smooth TiO$_2$ layers that are critically important to prevent formation of leakage paths to the ITO underneath.[19]

The TiO$_2$ films are examined by FT-IR, which show the suppression of stretching vibrations of the C–H moieties of the alkyl chain signals, thus proving the effective removal of the surface ligands (Fig. S2, ESI‡).

The OLAC/TOP-capped PbS QDs are deposited by spin-coating onto the ITO/TiO$_2$ substrate followed by dilute mercaptopropionic acid post-deposition treatment to remove the insulating ligands in order to increase the electronic coupling among nanoparticles as well as the carrier mobility within the PbS film.[26,27] By repeated spin-casting of QDs followed by mercapto-propionic treatments, we are able to control the thickness of the PbS layer and obtain a pinhole-free homogeneous morphology. Like for the TiO$_2$, the effectiveness of the mercaptopropionic treatment is verified by FT-IR studies (Fig. S3, ESI‡). In Fig. 2b we show a cross-sectional scanning electron microscopy (SEM) image of the TiO$_2$-NR–PbS-QD bi-layer. It can be readily observed that our post-deposition treatments lead to the formation of a

compact and net bi-layer film, which is favorable to obtain a good electric contact at the interfaces with the anode and cathode.

In Fig. 2c we show the current density *vs.* applied bias (*J–V*) characteristics under AM1.5 G (100 mW cm^{-2}) simulated solar illumination and in the dark for the TiO$_2$/PbS device. We obtain excellent performances, yielding a maximum power conversion efficiency of $\eta = 3.6\%$, a short circuit current $J_{SC} = 17.3$ mA cm^{-2}, a fill factor FF = 0.39 and an open circuit voltage $V_{OC} = 0.54$ V. In the inset of Fig. 2c, we report the incident photon to current efficiency (IPCE) and the normalized absorption spectra for this device. In both curves it is possible to distinguish the characteristic excitonic features of the PbS QDs. We use the IPCE measurement to estimate the total J_{SC} that would be generated under AM1.5 G (100 mW cm^{-2}) illumination conditions. We obtain a value of $J_{SC} = 16 \pm 1$ mA cm^{-2}, which indeed agrees, within the experimental error, with the J_{SC} measured using the solar simulator.

The higher V_{OC} compared to the state of the art Schottky[28] and depleted heterojunction DH bi-layer solar cells[10] can be due to existence of a good contact interface between the active layer and the anode/cathode electrodes, guaranteed by the smooth morphology of the TiO$_2$/PbS film, which allows most of the generated carriers to be efficiently separated in the depletion region. The built-in field drives the electrons to the ITO contact though the neutral region of TiO$_2$, whereas the holes diffuse to the MoO$_3$/Al anode. The smaller FF, compared to those achieved by similar heterojunctions, can be ascribed to surface traps in room-temperature processed TiO$_2$ NRs, originating from surface structural disorder or undercoordinated atoms.[29]

The high short circuit current, 17.3 mA cm^{-2}, can be attributed to the thin TiO$_2$–PbS bi-layer, that is 250 nm TiO$_2$ and 250 nm PbS. The thin TiO$_2$ layer ensures a better extraction of the photogenerated carriers formed in the depletion region, which could otherwise recombine along the path spanning from the edge of the depletion region to the electrodes. Moreover, a fraction of the light absorbed in the neutral region could be lost due to carrier recombination,[30] which can also negatively influence the V_{OC} in thicker devices. In Fig. S4 and Table S1 of the ESI‡ we report the *J–V* characteristics under illumination for different active layer thicknesses, which prove that a 250 nm/250 nm thick device offers the best compromise in terms of light absorption and charge recombination losses in the net bi-layer heterostructure.

Kelvin probe force microscopy (KPFM)

In order to verify whether the room-temperature post-deposition processing affects the materials optoelectronic properties and their interplay, especially at the interface, we have investigated the charge separation process in our system. First of all we have determined the relative position of the PbS and TiO$_2$ NC Fermi levels by KPFM measurements. The KPFM is a powerful technique that allows one to measure on the micrometer scale the Fermi level value relative to a reference surface; for our measurements a conductive Pt/Ir atomic force microscopy (AFM) tip and ITO contact are used as references. The measured work functions for the Pt/Ir tip and ITO are 4.8 eV and 4.7 eV

respectively. The relative Fermi level and band position values for the PbS and TiO$_2$ are sketched in Fig. S5.‡ In detail, the relative position of the valence band is calculated, on the basis of the known Fermi level of PbS, by the following equation:[31]

$$E'_v(\text{PbS}) = E'_f(\text{PbS}) + kT \ln \frac{p}{n_v}$$

where p, the effective hole density of the PbS QD layers, is assumed to be 10^{17} cm^{-3} (ref. 32) and n_v, the effective density of valence band states, is 2×10^{20} cm^{-3}. The relative conduction band $E'_c(\text{PbS})$ is determined by adding the energy gap value to the valence band, $E'_v(\text{PbS})$. The conduction band of TiO$_2$, $E_c(\text{TiO}_2)$, was taken from the literature and adjusted considering the work function of the reference ITO substrate. Our results show that the PbS QDs indeed form a type-II interface with TiO$_2$ NRs, which is critically important for an efficient charge separation process. Moreover the difference in the quasi-Fermi level of electrons and holes in n-type TiO$_2$ and p-type PbS NCs is 0.53 eV (Fig. S5‡), which is in accordance with the value reported in the literature for nanoporous TiO$_2$.[9] The built-in-voltage, that equals the difference in the Fermi levels across the n–p junction, is similar in magnitude to the V_{OC} value measured for our device. This is consistent with the picture of a built-in-field that can efficiently drive the separation photogenerated charge carriers in an n–p junction device.[33]

The charge separation process can be directly visualized by mapping the surface potential of ITO/PbS-QD (Fig. S6a and b‡) and ITO/TiO$_2$-NR/PbS-QD (Fig. 3a and b) devices by KPFM in the dark and under illumination.[34] The potential shift is measured under three different conditions: (i) before illumination (labeled "dark-1"), (ii) under illumination (labeled "light"), and (iii) after illumination (labeled "dark-2") with a white light source (Fig. 3c). Surface potentials (Fig. 3a and b) have been calculated from $\Delta\text{SP} = \Pi_{\text{sample}} - \Pi_{\text{tip}}$[35,36] measured by

calibrating the cantilever on a HOPG reference sample.[37] For comparison the AFM morphology is also reported in Fig. 3d.
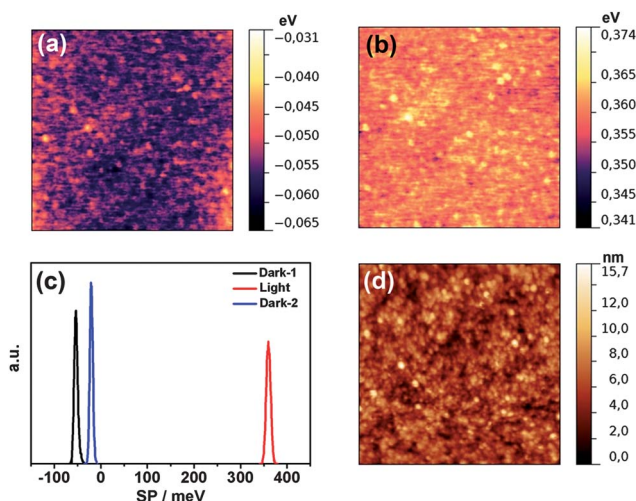
The surface potential images of the ITO/TiO$_2$-NR/PbS-QD sample in the dark (Fig. 3a) show darker and brighter regions. Since charges are thought to be absent in the dark, the surface potential should be equal to the work function difference between the tip and the ITO electrode. In our experiment the measured ITO work function $\Pi_{\text{ITO}} = 4.7$ eV and the difference $\Pi_{\text{ITO}} - \Pi_{\text{Tip}} \approx -110$ meV. In the dark (Fig. 3a) the sample shows a surface potential distribution with the center near to the Fermi level values of the ITO electrode and weak contrast in the surface potential difference. The potential shift relative to the ITO Fermi level is 57 meV. Under dark conditions, this is probably due to the vacuum level shift at the interface of the TiO$_2$ NRs with the bottom ITO electrode.[38] In the dark, Fermi level pinning occurs for the ITO–PbS-QD interface, as reported in the ESI‡ (Fig. S5 and S6).

Under illumination a photovoltaic effect occurs leading to a positive shift in the surface potential of both structures. Fig. 3c clearly shows an increase of the surface potential due to hole excess on the surface after charge dissociation at the double layer interfaces. The quantity $\text{SP}_{\text{light–dark}} = \text{SP}_{\text{light}} - \text{SP}_{\text{dark}}$ for ITO/TiO$_2$-NRs/PbS-QDs and ITO/PbS-QDs is 413 meV and 221 meV respectively. The increase of the $\text{SP}_{\text{light–dark}}$ reflects the presence of the TiO$_2$ bottom layer acting as an electron extraction layer, thanks to the low electron extraction barrier, as reported in Fig. S5.‡ The KPFM results underline that our room-temperature treatments allow us to obtain a good contact between the donor and acceptor at the n–p junction, leading to efficient photoinduced electron–hole pair separation.
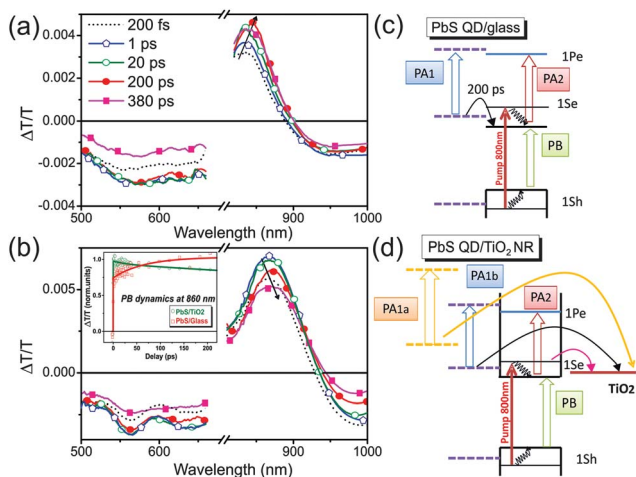
Ultrafast transient absorption

In order to selectively address the process of charge generation at the interface, we performed ultrafast transient absorption (TA) spectroscopy measurements.[39,40] For comparison the TA spectral evolution of the PbS QDs deposited on glass and on TiO$_2$ NRs is shown in Fig. 4a and b.

The TA spectrum of the PbS QDs on glass shows a positive fractional change in transmission peaked at 850 nm. It is assigned to the PbS photobleaching (PB) due to the state filling of the 1S state. The signal shows a rise in the first 200 ps (see inset of Fig. 4b). At wavelengths shorter than 680 nm a broad photo-induced absorption (PA$_1$) band appears. It starts decaying tens of ps after photoexcitation, mirroring the PB rise (see the dynamics in Fig. S7 in the ESI‡). At wavelengths longer than 900 nm a second broad photo-induced absorption (PA$_2$) band appears. It shows an initial fast decay ($\tau \sim 1$ ps) and a second long lived component. We rationalize the depicted scenario with the help of the energy levels of the cartoon presented in Fig. 4c. We assign PA$_1$ to the population of QD surface traps within the first few ps (see Fig. 4a). These carriers can partially relax in the QDs after the first 200 ps, feeding the 1Se state, as the delayed rise in the PB demonstrates. On the other hand, PA$_2$ can be associated with the superposition of two processes, a Stark effect and an inter-band transition of electrons from 1Se to 1Pe states with energy around 1 eV.[41,42]

Fig. 3 Surface potential image of the ITO/TiO$_2$-NR/PbS-QD device (a) in the dark and (b) under illumination. (c) Histogram distribution of the surface potential under three different conditions: before illumination (labeled "dark-1"), under illumination (labeled "light"), and after illumination (labeled "dark-2"). (d) AFM image of the ITO/TiO$_2$-NR/PbS-QD sample. The scan size of the AFM and surface potential images is 2 μm × 2 μm.

Fig. 4 Transient absorption spectra at selected pump probe delays of PbS QDs on a glass substrate (a) and of TiO_2-NRs/PbS-QDs (b). (c) and (d) Cartoons of the energy levels and photophysical processes of the PbS QD/glass and of the PbS QDs on TiO_2 NRs.

When the PbS QDs are deposited on the TiO_2 NRs, the physical scenario changes as interface phenomena take place. First of all, the PB band appears to be much broader, extending up to 950 nm and its dynamics is different, showing a decay in the first 200 ps (see the inset in Fig. 4b). PA_2 shows a faster initial decay due to Stark effect (see dynamics in Fig. S7 in the ESI‡), followed by a slower component of about 200 ps which again mirrors the PB band behavior. On the other side, the PA_1 band results in being more structured, with a more defined sub-band centered at 550 nm (PA_{1a}) and a broader band centered at 630 nm (PA_{1b}). Considering the small dispersion in QD size, we can exclude that the PB broadening derives from inhomogeneous distribution, and assign it to a strong TiO_2-NR–PbS-QD interaction.[43] Indeed, the 1Se level of the QDs, as shown in the inset of Fig. 1b, is located above the TiO_2 CB edge. Due to the strong confinement of the QDs, the electron wavefunction can extend beyond the QD surface, leading to mixing with the CB levels of the TiO_2 and partial delocalization of the carriers. This proves the efficacy of the room-temperature treatments introduced in the fabrication. The strong interaction of TiO_2-NR–PbS-QD at the interface leads to an efficient electron transfer process, as demonstrated by the quicker decay of the PB and PA_2 band. On the other side, PA_{1a} and PA_{1b} still reveal the presence of trap states on the QD surface. We assign PA_{1a}, which is formed within our time resolution ($t < 200$ fs), to a hybrid interfacial state at the TiO_2-NR–PbS-QD junction site; while we assign PA_{1b} to a pure QD surface state. The latter shows an initial fast decay (in the first few ps) followed by a slower rise in the first 20 ps (mirroring the PB) which could be attributed to a direct electron transfer from the surface state to the TiO_2 and a residual feed of the 1Se level which could be delayed by charge diffusion on the surface. Finally we observe that both PA_{1a} and PA_{1b} decay are slower with respect to the PA_1 decay observed when the QDs are deposited on glass, and do not match with the PB dynamics. This may indicate that the surface states do not feed anymore the 1Se level, but might reach the TiO_2 interface after a diffusion process.

In summary, the spectroscopic results demonstrate that efficient electron transfer occurs via several pathways in a time range from 200 fs to hundreds of ps: (1) direct electron injection from the 1Se level to the levels in the TiO_2 CB; (2) fast injection through hybrid interfacial states instantaneously formed at the TiO_2-NR–PbS-QD hetero-interface; (3) electron transfer from the surface states of the QDs upon diffusion (within the hundreds of ps timescale, depending on the relative distance between the QD state and the TiO_2 NR).

Flexible all-inorganic solar cells

Finally, we have fabricated TiO_2/PbS solar cells on an ITO-coated PET substrate (inset, Fig. 5).

The device characteristics in the dark and under illumination are reported in Fig. 5, corresponding to $V_{OC} = 0.37$ V, $J_{SC} = 14.8$ mA cm^{-2}, FF = 0.33 and a power conversion efficiency of $\eta = 1.8\%$, which is the highest reported for flexible all-NC-based solar cells. The IPCE spectrum for the same device is shown in Fig. S8 of the ESI.‡ The lower performance when compared with the ones fabricated on the conventional ITO glass substrate is probably due to differences in the ITO quality and roughness. Indeed, it is well established that the quality of the ITO deposition on plastic can negatively influence the sheet resistance and change its work function.[44,45] Transparent conductive oxide growth on plastic remains a significant challenge because of the poor thermal and mechanical properties of polymeric substrates. The growth of a good quality ITO film requires relatively high deposition and/or post-annealing temperature (>200 °C) to achieve appreciable electrical conductivity, optical transparency and long-term stability. Generally ITO film growth on plastic must be carried out at significantly lower temperatures, inevitably resulting in poorer conductivity, morphological transparency and adhesion properties, which ultimately lead to
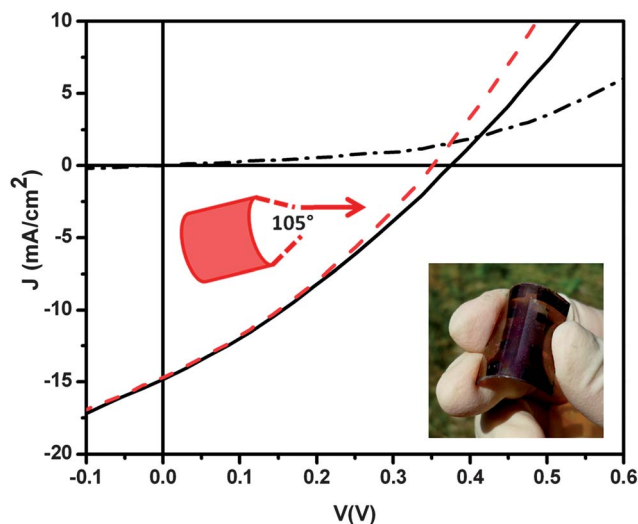
Fig. 5 TiO_2-NR/PbS-QD NC photovoltaic devices on a plastic substrate. Current density–voltage characteristics of the photovoltaic device under zero illumination (dash-dotted curve) and standard illumination when flat (continuous curve, 1.8% power conversion efficiency) and released to flat after bent to a curvature of 105° (dashed curve, 1.7% power conversion efficiency). Inset: photograph of the TiO_2-NR/PbS-QD plastic solar cell.

reduced device quality.[46] The higher roughness of ITO can provoke charge carrier losses at the electrode and increase of leakage current.[47,48]

A comparison of performance recorded when the device is originally flat (continuous curve, Fig. 5) *versus* released to flat after bent to a curvature of 105° (dashed curve, Fig. 5) shows that there is only a small change after the bending. A slight decrease in open circuit voltage ($V_{OC} = 0.35$ V) and short circuit current ($J_{SC} = 14.7$ mA cm^{-2}) for the device after the bending is observed, corresponding to an overall decrease of power efficiency to 1.7%.

This change is small (~6%), given the large stress on the device during bending, and clearly underlines the robust nature of our NC/plastic solar cells and their potential as power sources for flexible hand-held consumer electronics.

Conclusions

In summary, we successfully demonstrate fully inorganic colloidal NC solar cells fabricated by room-temperature processing compatible with plastic technology. We achieved the highest power conversion efficiency of 1.8% for the device fabricated on plastic and 3.6% for that on glass. In the future, the efficiency of the PbS–TiO$_2$ heterojunction device may be improved by increasing the active surface area for charge separation by blending the preformed donor/acceptor NCs or by enhancing their surface passivation so as to minimize midgap states and traps.

Through femtosecond pump and probe and KPFM measurements we demonstrate that our room-temperature treatments still allow for a strong interaction at the TiO$_2$-NR–PbS-QD interface, which in turn leads to high performance devices. We find a multi-step electron transfer process taking place from $t < 200$ fs to hundreds of ps. Our fabrication method represents a step forward toward all-inorganic and stable nanocrystal-based devices for low-cost power conversion on flexible substrates. In view of the energy cost associated with conventional solar cell manufacturing, a room-temperature solution-processing approach could potentially reduce the production cost and in turn the energy payback time.

Experimental

Nanocrystal synthesis

All syntheses were carried out under nitrogen flow using a standard Schlenk line set-up.

Synthesis TiO$_2$ NRs

Oleate-capped anatase TiO$_2$ NRs were obtained by low-temperature TMAO catalyzed hydrolysis of TTIP in OLAC at 100 °C.[21] The NRs separated from their growing mixture upon addition of 2-propanol and were subsequently subjected to repeated cycles of re-suspension in toluene and precipitation with acetone to wash out surfactant residuals. The as-purified NRs were then dispersed in chloroform.

Synthesis of PbS QDs

The preparation of PbS QDs was carried out as previously reported.[22] In a typical synthesis, 4 mmol of PbO, 3.0 mL of trioctylphosphine (TOP), and 2.7 mol of oleic acid (OLAC) were added to 36 mL of 1-octadecene (ODE), a noncoordinating solvent, and stirred under vacuum at 120 °C: at this stage the formation of lead-oleate precursors occurred. Subsequently, a 20 mM solution of the sulfur precursor, hexamethyldisilathiane (HMDS) in ODE, was swiftly injected, corresponding to a Pb/S molar ratio equal to 2 : 1, followed by cooling to 80 °C in order to stop the nucleation and let the freshly formed nuclei grow. The reaction was stopped after 10 minutes and the obtained QDs were purified by using a nonsolvent precipitation procedure, carried out by adding to the reaction product a large amount of a short alkyl chain alcohol (ethanol). In order to completely remove the excess of OLAC and other impurities formed during the reaction up to 3 centrifugation steps were required, finally yielding a powder. The obtained precipitate was then dispersed in toluene.

Device preparation

TiO$_2$ NR coatings were fabricated under ambient laboratory conditions as follows. A solution of purified TiO$_2$ NRs in CHCl$_3$ was spin-coated onto patterned ITO cleaned substrates at 1500 rpm for 60 s to form a TiO$_2$ layer of ~50 nm. The TiO$_2$ coatings were irradiated with a continuous wave-UV (cw-UV) lamp (SPECTROLINE E-Series Ultraviolet hand Lamps with excitation wavelength centered at 365 nm) positioned at a distance of 5 cm from the sample. Afterwards, chloroform was dispensed on top of the film and then spin-cast to remove possible organic residuals (undetectable by FT-IR). This protocol constituted one cycle of the 'sequential spin-coated' procedure to fabricate a robust TiO$_2$ film of ~250 nm.

The as-synthesized PbS QDs (1 eV) in toluene were re-dispersed in the higher boiling point solvent octane to obtain a smoother film at a concentration of 22 mg mL^{-1}. The PbS QDs in octane were deposited in a layer-by-layer (LBL) fashion. Three drops of QDs were dispensed onto the substrates through a 0.2 μm filter and spin-cast at 2500 rpm for 10 seconds; eight drops of a 0.2% mercaptopropionic acid in methanol solution were applied to the CQD film for 3 seconds, then spin-cast at 2500 rpm. Finally, three rinsing steps were carried out: with methanol, with acetone and the final one with octane, each followed by spinning of the substrate at 2500 rpm for 10 seconds. This procedure was repeated until the desired film thickness (~250 nm) was obtained (10 cycles). The PbS film was then loaded into the evaporation chamber. The MoO$_3$ was thermally evaporated at a rate of 0.5 Å s^{-1} at a base pressure of ~10^{-6} Torr. The final thickness of MoO$_3$, unless otherwise noted, was 10 ± 1 nm. The evaporation sources were acquired from Aldrich (99.99% molybdenum oxide). Finally, the Al electrode (~100 nm) was thermally evaporated. The active area of the device, 4 mm^2, has been accurately determined using an optical microscope, using a 4× magnification objective equipped with a ruler. Current density *versus* voltage (*J*–*V*) measurements were performed with an Air Mass 1.5 Global (AM1.5 G) solar

simulator with an irradiation intensity of 100 mW cm^{-2}. All the fabrication processes were carried out in a glovebox. EQE data were acquired in air by using an encapsulated device. A calibrated filtered Si diode (Newport, 91150V) served as the reference cell for J–V measurements.

KPFM measurements

KPFM images were acquired with a commercial AFM system (Bruker-AXS) MultiMode AFM with a Nanoscope V controller operating in Lift Mode (typical lift height 20 nm) by using silicon tips with a PtIr coating (SCM-PIT) with $k \approx 3$ N m^{-1}, tip radius ≈ 20 nm, and resonant frequency ≈ 80 kHz. Surface potential maps were acquired in the dark and under illumination by means of a halogen lamp, with an estimated power density on the sample of 0.45 kW m^{-2}.

Transient absorption measurements

In transient absorption measurements, commonly referred to as the "pump–probe" experiment, a short pump pulse is used to selectively photoexcite the molecule. The subsequent dynamical evolution of the photoexcited states is monitored by a delayed weaker and broadband probe beam. The signal measured represents the normalized differential transmission induced by the probe as a function of pump–probe delay τ and probe wavelength λ: $\Delta T/T = [(T_{pump\_on} - T_{pump\_off})/T_{pump\_off}]$. A regenerative amplified mode locked Ti:sapphire laser (Clark-MXR Model CPA-1)^{39,40} delivers the laser pulse train at 1 kHz repetition rate, centered at $\lambda = 780$ nm wavelength with 150 fs duration. A fraction of this beam is used as the excitation pulse tuned either at 780 nm or, by doubling its frequency *via* a second harmonic process in a non-linear crystal, at 390 nm wavelength. Another small fraction of the Ti:sapphire amplified output is focused into a 2 mm thick sapphire plate to generate a stable single-filament white-light supercontinuum, which serves as a broadband probe pulse, spanning from the 400 nm to 1000 nm spectral region. The pump and probe beams are spatially overlapped on the sample, and their relative delay is optically adjusted by a motorized slit with 5 nm accuracy. The system has a sensitivity of around $\Delta T/T \sim 10^{-4}$ with a $\sim$150 fs temporal resolution. Details of the experimental set-up can be found elsewhere.^{39,40} The pump beam density energy used in the experiment has been kept deliberately low (of around 10 μJ cm^{-2}). All the measurements were taken with the samples in a vacuum chamber, to prevent any influence from oxygen or sample degradation.

Acknowledgements

Notes and references

1 J. M. Luther, M. Law, M. C. Beard, Q. Song, M. O. Reese, R. J. Ellingson and A. J. Nozik, *Nano Lett.*, 2008, **8**, 3488–3492.

2 J. Tang and E. H. Sargent, *Adv. Mater.*, 2011, **23**, 12–29.

3 J. Tang, X. Wang, L. Brzozowski, D. A. R. Barkhouse, R. Debnath, L. Levina and E. H. Sargent, *Adv. Mater.*, 2010, **22**, 1398–1402.

4 J. J. Choi, Y. Lim, M. B. Santiago-Berrios, M. Oh, B. Hyun, L. Sun, A. C. Bartnik, A. Goedhart, G. G. Malliaras, H. D. Abrunal, F. W. Wise and T. Hanrath, *Nano Lett.*, 2009, **9**, 3749–3755.

5 E. H. Sargent, *Nat. Photonics*, 2012, **6**, 133–135.

6 R. Mastria, A. Rizzo, C. Nobile, S. Kumar, G. Maruccio and G. Gigli, *Nanotechnology*, 2012, **23**, 305403–305411.

7 E. H. Sargent, *Nat. Photonics*, 2009, **3**, 325–331.

8 M. Grätzel, R. A. J. Janssen, D. B. Mitzi and E. H. Sargent, *Nature*, 2012, **488**, 304–312.

9 A. G. Pattantyus-Abraham, I. J. Kramer, A. R. Barkhouse, X. Wang, G. Konstantatos, R. Debnath, L. Levina, I. Raabe, M. K. Nazeeruddin, M. Grätzel and E. H. Sargent, *ACS Nano*, 2010, **4**, 3374–3380.

10 H. Liu, J. Tang, I. J. Kramer, R. Debnath, G. I. Koleilat, X. Wang, A. Fisher, R. Li, L. Brzozowski, L. Levina and E. H. Sargent, *Adv. Mater.*, 2011, **23**, 3832–3837.

11 D. A. R. Barkhouse, R. Debnath, I. J. Kramer, D. Zhitomirsky, A. G. Pattantyus-Abraham, L. Levina, L. Etgar, M. Grätzel and E. H. Sargent, *Adv. Mater.*, 2011, **28**, 3134–3138.

12 J. Tang, K. W. Kemp, S. Hoogland, K. S. Jeong, H. Liu, L. Levina, M. Furukawa, X. Wang, X. Debnath, D. Cha, K. W. Chou, A. Fischer, A. Amassian, J. B. Asbury and E. H. Sargent, *Nat. Mater.*, 2011, **10**, 765–771.

13 X. Wang, G. I. Koleilat, J. Tang, H. Liu, I. J. Kramer, R. Debnath, L. Brzozowski, D. A. R. Barkhouse, L. Levina, S. Hoogland and E. H. Sargent, *Nat. Photonics*, 2011, **5**, 480–484.

14 A. H. Ip, S. M. Thon, S. Hoogland, O. Voznyy, D. Zhitomirsky, R. Debnath, L. Levina, L. R. Rollny, G. H. Carey, A. Fischer, K. W. Kemp, I. J. Kramer, Z. Ning, A. J. Labelle, K. W. Chou, A. Amassian and E. H. Sargent, *Nat. Nanotechnol.*, 2012, **7**, 577–582.

15 G. I. Koleilat, X. Wang, A. J. Labelle, A. H. Ip, G. H. Carey, A. Fischer, L. Levina, L. Brzozowski and E. H. Sargent, *Nano Lett.*, 2011, **11**, 5173–5178.

16 J. Gao, J. M. Luther, O. E. Semonin, R. J. Ellingson, A. J. Nozik and M. C. Beard, *Nano Lett.*, 2011, **11**, 1002–1008.

This journal is © The Royal Society of Chemistry 2013

Energy Environ. Sci., 2013, **6**, 1565–1572 | **1571**

17 A. K. Rath, M. Bernechea, L. Martinez, F. P. Garcia de Arquer and J. O. G. Konstantatos, *Nat. Photonics*, 2012, **6**, 529–534.

18 I. Gur, N. A. Fromer, M. Geier and A. Paul Alivisatos, *Science*, 2005, **310**, 462–465.

19 A. Loiudice, A. Rizzo, L. De Marco, M. R. Belviso, G. Caputo, P. D. Cozzoli and G. Gigli, *Phys. Chem. Chem. Phys.*, 2012, **14**, 3987–3995.

20 Y. Wu, C. Wadia, W. Ma, B. Sadler and A. Paul Alivisatos, *Nano Lett.*, 2008, **8**, 2551–2555.

21 P. D. Cozzoli, A. Kornowski and H. Weller, *J. Am. Chem. Soc.*, 2003, **125**, 14539–14548.

22 M. Corricelli, D. Altamura, L. De Caro, A. Guagliardi, A. Falqui, A. Genovese, A. Agostiano, C. Giannini, M. Striccoli and M. L. Curri, *CrystEngComm*, 2011, **13**, 3988–3997.

23 N. Herron, J. C. Calabrese, W. E. Farneth and Y. Wang, *Science*, 1993, **259**, 1426–1428.

24 I. Moreels, K. Lambert, D. Smeets, D. De Muynck, T. Nollet, J. C. Martins, F. Vanhaecke, A. Vantomme, C. Delerue, G. Allan and Z. Hens, *ACS Nano*, 2009, **3**, 3023–3030.

25 B.-R. Hyun, Y.-W. Zhong, A. C. Bartnik, L. Sun, H. D. Abrun, F. W. Wise, J. D. Goodreau, J. R. Matthews, T. M. Leslie and N. F. Borrelli, *ACS Nano*, 2008, **2**, 2206–2212.

26 J. M. Luther, M. Law, Q. Song, C. L. Perkins, M. C. Beard and A. J. Nozik, *ACS Nano*, 2008, **2**, 271–280.

27 Y. Liu, M. Gibbs, J. Puthussery, S. Gaik, R. Ihly, H. W. Hillhouse and M. Law, *Nano Lett.*, 2010, **10**, 1960–1969.

28 R. Debnath, J. Tang, D. A. Barkhouse, X. Wang, A. G. Pattantyus-Abraham, L. Brzozowski, L. Levina and E. H. Sargent, *J. Am. Chem. Soc.*, 2010, **132**, 5952–5953.

29 J. Bouclé, S. Chyla, M. S. P. Shaffer, J. R. Durrant, D. D. C. Bradley and J. Nelson, *Adv. Funct. Mater.*, 2008, **18**, 622–633.

30 K. W. Johnston, A. G. Pattantyus-Abraham, J. P. Clifford, S. H. Myrskog, D. D. MacNeil, L. Levina and E. H. Sargent, *Appl. Phys. Lett.*, 2008, **92**, 122111–122115.

31 S. M. Sze and K. K. Ng, *Physics of Semiconductor Devices*, John Wiley & Sons, Inc., Hoboken, NJ, 3rd edn, 2007.

32 E. J. D. Klem, H. Shukla, S. Hinds, D. D. MacNeil, L. Levina and E. H. Sargent, *Appl. Phys. Lett.*, 2008, **92**, 212102–212105.

33 R. Debnath, O. Bakr and E. H. Sargent, *Energy Environ. Sci.*, 2011, **4**, 4870–4881.

34 G. Grancini, M. Biasiucci, R. Mastria, F. Scotognella, F. Tassone, D. Polli, G. Gigli and G. Lanzani, *J. Phys. Chem. Lett.*, 2012, **3**, 517–523.

35 M. Chiesa, L. Burgi, J.-S. Kim, R. Shikler, R. H. Friend and H. Sirringhaus, *Nano Lett.*, 2005, **5**, 559–563.

36 H. Hoppe, T. Glatzel, M. Niggemann, A. Hinsh, M. C. Lux-Steiner and N. S. Sariciftci, *Thin Solid Films*, 2006, **511**, 587–592.

37 A. Loiudice, A. Rizzo, M. Biasiucci and G. Gigli, *J. Phys. Chem. Lett.*, 2012, **3**, 1908–1915.

38 K. Maturovà, M. Kemerink, M. M. Wienk, D. S. H. Charrier and R. A. J. Janssen, *Adv. Funct. Mater.*, 2009, **19**, 1379–1386.

39 G. Lanzani, G. Cerullo, D. Polli, A. Gambetta, M. Zavelani-Rossi and C. Gadermaier, *Phys. Status Solidi A*, 2004, **201**, 1116–1131.

40 J. Cabanillas-Gonzalez, G. Grancini and G. Lanzani, *Adv. Mater.*, 2011, **23**, 5468–5485.

41 M. R. Antognazza, F. Scotognella, K. Miszta, D. Dorfs, M. Zanella, M. Zavelani-Rossi, L. Manna, G. Lanzani and F. Tassone, *Phys. Chem. Chem. Phys.*, 2011, **13**, 15326–15330.

42 F. Scotognella, K. Miszta, D. Dorfs, M. Zavelani-Rossi, R. Brescia, S. Marras, L. Manna, G. Lanzani and F. Tassone, *J. Phys. Chem. C*, 2011, **115**(18), 9005–9011.

43 Y. Yang, W. Rodrìguez-Cordoba, X. Xiang and T. Lian, *Nano Lett.*, 2012, **12**, 303–309.

44 I. Elfallal, R. D. Pilkington and A. E. Hill, *Thin Solid Films*, 1993, **223**, 303–310.

45 R. N. Chauhan, C. Singh, R. S. Anand and J. Kumar, *Int. J. Photoenergy*, 2012, **2012**, 879261.

46 J. Huang, X. Wang, Y. Kim, A. J. deMello, D. D. C. Bradley and J. C. deMello, *Phys. Chem. Chem. Phys.*, 2006, **8**, 3904–3908.

47 S. Günes, H. Neugebauer and N. S. Sariciftci, *Chem. Rev.*, 2007, **107**, 1324–1338.

48 F. Z. Dahou, L. Cattin, J. Garnier, J. Ouerfelli, M. Morsli, G. Louarn, A. Bouteville, A. Khellil and J. C. Bernède, *Thin Solid Films*, 2010, **518**, 6117–6122.